



Numerical Cutting Simulation and Experimental Investigations on Determining the Minimum Uncut Chip Thickness of PTFE

Zhi Cui¹ · Jing Ni¹ · Lihua He^{1,2} · Zefei Zhu¹ · Bokai Lou¹ · Jinda Liao¹

Received: 15 February 2024 / Revised: 28 April 2024 / Accepted: 29 April 2024
© The Author(s), under exclusive licence to Korean Society for Precision Engineering 2024

Abstract

Polytetrafluoroethylene (PTFE) has become an essential material in the manufacturing of critical flow-control components in various industries. These components require high surface quality and micron-level machining dimensions. The study of the minimum uncut chip thickness (MUCT) presents an opportunity to enhance the machining precision of PTFE. The objective of the research is to determine the MUCT of PTFE by employing finite element (FE) cutting simulation and orthogonal cutting experiments. Initially, the two-dimensional orthogonal FE cutting models, with varying parameters of cutting depth (30–80 μm) and cutting speed (5000 mm/min), utilizing the Johnson–Cook (J–C) constitutive model has been applied for simulating the MUCT of PTFE. The parameters of the J–C constitutive model have been determined through quasi-static tension tests (Strain rates: 0.001 s^{-1} – 0.1 s^{-1} , Temperature: $24\text{ }^\circ\text{C}$) and the split Hopkinson bar (SHPB) tests (Strain rates: 500 s^{-1} – 3000 s^{-1} , Temperature: 24 – $100\text{ }^\circ\text{C}$). Subsequently, the orthogonal cutting experiments corresponding to the FE simulation are designed and performed. The cutting force, cutting chip, and machined surface morphology are analyzed to assess the precision of the established FE model and determine the MUCT of PTFE. It was concluded that the numerical results are in good agreement with the experimental results, with a minimum relative error of 0.885% in cutting force and 2.03% in the axial ratio of chip curvature. And the MUCT for PTFE was determined to be $70\text{ }\mu\text{m}$ in this study, in the case of rake angle, flank angle, and tool edge radius of the cutting tool are 0° , 6° , and $40\text{ }\mu\text{m}$, respectively. It has been indicated that the properties and flow direction of the removed workpiece material play a significant role in chip formation under the influence of extrusion and friction in the workpiece-tool-chip contact area. These results offer a theoretical foundation for enhancing the machining precision of PTFE.

Keywords PTFE · Finite element simulations · Johnson–Cook model · Minimum uncut chip thickness · Cutting

List of Symbols

σ	Equivalent stress	$\dot{\epsilon}_0$	Reference strain rate
A	Initial flow stress	T	Temperature
B	Hardening modulus	T_0	Reference temperature
C	Strain rate dependency coefficient	T_{melt}	Melting temperature
n	Work-hardening exponent	φ	Diameter of specimen for SHPB test
m	Thermal softening coefficient	l_s	Length of specimen for SHPB test
ϵ_p^n	Equivalent plastic strain	α	Rake angle of cutting tool
$\dot{\epsilon}$	Equivalent plastic strain rate	γ	Flank angle of cutting tool
		λ	Inclination angle of cutting tool
		r	Tool radius
		f	Tool feed
		a_p	Cutting depth
		v	Cutting velocity
		F_x	Main cutting force
		t	Cutting time

✉ Jing Ni
nj2000@hdu.edu.cn

✉ Lihua He
helihua0617@hdu.edu.cn

¹ School of Mechanical Engineering, Hangzhou Dianzi University, Hangzhou 310018, China

² State Key Laboratory of Fluid Power and Mechatronic Systems, Zhejiang University, Hangzhou 310027, China

1 Introduction

Polytetrafluoroethylene (PTFE) has emerged as an essential material for flow control components in wafer cleaning equipment and wet chemical etching equipment, owing to its exceptional corrosion resistance and high-temperature endurance [1]. PTFE parts with simple geometries are often produced by compression molding, and sintering techniques [2, 3]. Mechanical cutting operations are also required to produce some PTFE parts with complex geometries. The machining dimension of some parts reaches the micron level. However, the cutting mechanisms of PTFE are significantly different from metal cutting in terms of chip formation, and surface quality. And it is difficult to ensure machining accuracy during cutting PTFE because of its properties such as low strength, high elasticity, and large linear expansion coefficient [4]. So, it is necessary to investigate the cutting mechanisms of PTFE, which is crucial for promoting its machining accuracy.

The knowledge of minimum uncut chip thickness (MUCT) is an efficient way to investigate the cutting mechanisms and select the appropriate cutting conditions. Liu et al. [5] reported that, in orthogonal cutting, there are no chips generated when the cutting depth keeps below a critical value, and the plowing effect is the main factor affecting the cutting process. The MUCT effect would limit the machined surface quality. When the cutting depth exceeded the critical value, the chips will be formed. This critical value is defined as the MUCT. When the uncut chip thickness is nearby or less than the MUCT, the surface roughness is mainly attributed to the plowing effect [6]. So, the MUCT is a measure of machining accuracy gainable in the ideal conditions with ideal machine and tool performance [7].

The MUCT is dependent on the workpiece material and cutting tool geometries [8]. Many experimental methods have been used to determine the MUCT of different cutting processes. De Oliveira et al. [9] performed milling tests on AISI 1045 steel in the case of cutting depth varied from 80 to 320 μm . And they determined the MUCT by correlating the cutting force, chip formation, and surface roughness. Yun et al. [10] presented a method, which could detect the MUCT during cutting copper by analyzing the peak values of the cutting force signal. Rezaei et al. [11] evaluated the MUCT of Ti-6Al-4V during the milling process both quantitatively and qualitatively by analyzing the machined surfaced surface quality and the cutting force. They concluded the MUCT varied in the range of 15% to 49% of the tool edge radius. In addition, some newer approaches such as finite elements methods, and smoothed particle hydrodynamics have been applied for the determination of MUCT [12].

The FE cutting simulation is the most generalized method in modeling the cutting process, which is efficient and low in cost. FEM could reveal the distribution of strains, strain rates, and temperatures of the cutting process simultaneously [13]. To predict the cutting process accurately, the parameters of the material constitutive model should be determined precisely with the appropriate methods. The J–C constitutive model, which could reflect the quasi-static and dynamic properties of the materials, is commonly used in describing the constitutive behavior of the materials during the cutting process [14]. In this regard, quasi-static tension/compression experiments, SHPB tests, and cutting tests are commonly used methods to identify the parameters of the J–C constitutive model [15–18].

In recent years, a large sum of research has been conducted to identify the constitutive parameters of polymers, composites, and metals. And a variety of FE models for cutting these materials have been established. Rae and Dattelbaum [19] conducted the quasi-static compression tests of PTFE with strain rates varied from 10^{-4} to 1 s^{-1} , and SHPB compression tests of PTFE under the strain rate at 3200 s^{-1} with different temperatures. Then, Rae and Brown [20] conducted a series of tension tests of PTFE under various conditions. They concluded that the mechanical properties of PTFE were mainly affected by strain rate and temperature. Yan et al. [21] tested the dynamic mechanical properties of titanium alloy by high-temperature SHPB experiments, and the sensitivity of strain and temperature of titanium alloy were analyzed by the true strain–stress curves. In addition, they used the power-law and the J–C constitutive model to fit the experimental results. The average error of both models with the experimental results was less than 6%.

Yang et al. [22] proposed an explicit FE model to predict the cutting performance of high-density polyethylene (HDPE). The J–C constitutive was established based on the true stress–strain curve, and the chip formation processes were simulated based on the ductile damage criterion. Fu et al. [23] also used the ductile damage model to simulate the fracture of the epoxy materials during the macro-machining process (cutting depth varies from 10 to 100 μm). They concluded that the shear plastic slip mechanism could describe the epoxy cutting deformation. Fan et al. [24] conducted a series of compression tests with different strain rates and temperatures to identify the J–C constitutive parameters of SiCp/Al composites. They modified the constitutive model by considering the strain gradient theory. And they concluded that the cutting mechanism of SiCp/Al composites could be better revealed by the modified constitutive model. Lu et al. [25] conducted ultra-precision grooving experiments on SiCp/Al composites, and the chip profile captured by the high-speed camera and the simulation results were in good agreement. Bagheri et al. [26] determined the effect of friction stir processing (FSP) parameters and vibration on

the machining behavior of AZ91 alloy by establishing the three-dimensional FE modeling for simulating the small-hole drilling process of AZ91 alloy incorporating J–C constitutive model and material failure criterion. The results of chip formation, chip morphology, and cutting forces show that the application of vibration during the friction stir processing (FSP) improves adiabatic shearing and thus leads to more discontinuous chips, which finally enhances the mechanical and machining properties of processed AZ91 alloy.

Teng et al. [27] compared the accuracy of the smoothed particle hydrodynamics (SPH)-FEM coupling cutting model and the FE cutting model during SiC/Al matrix composites cutting simulation. And the established model has been verified by the orthogonal cutting experiments. The results showed that the SPH-FEM model had higher accuracy in predicting the cutting performance. Saelzer et al. [28] identified the parameters of the J–C constitutive model by temperature-dependent experiments and the covariance matrix adaptation evolution strategy. The results of the orthogonal FE cutting simulations showed that the coupled approach could predict the cutting force more accurately. Elkaseer et al. [29] reported the results of a FEM modeling and simulation study during cutting of stainless steel 316L in the case of cutting depth was 0.01 mm with different feed rates. And the results of the simulation and experimental were compared by the morphologies of chips. Moreover, the geometries of the cutting tool are considered to be one of the most critical parameters in the orthogonal cutting process. In the orthogonal cutting FE simulation and experiments, the cutting deformation could be well analyzed by setting the rake angle as 0° [30, 31]. Further, compared with other rake angles, performing the orthogonal cutting FE simulation by setting the tool model with rake angle of 0° could predict the actual cutting results more accurately [32].

The aforementioned literature indicates that substantial numerical and experimental investigations have been conducted to assess the MUCT of polymers, metals, and composite materials. Furthermore, FE models have been developed and verified for cutting these materials. But limited research has been carried out on cutting PTFE. In this paper, the parameters of the J–C constitutive model for PTFE have been identified by conducting quasi-static tension tests and the SHP tests under different strain rates and temperatures. The two-dimensional orthogonal FE cutting models utilizing the J–C constitutive model with varying cutting depths, and the corresponding orthogonal cutting experiments have been performed. The study compares numerical and experimental results of cutting force, chip formation, and machined surface morphology to validate the accuracy of the established FE model and determine the MUCT of PTFE. Additionally, the Mises stress within the tool-workpiece contact area and the displacement vector diagram of workpiece surface

nodes in simulation are analyzed to investigate the characteristics of chip formation as the cutting depth approaches the MUCT.

2 Identification of Materials Parameters

Johnson–Cook constitutive model, which is developed by Johnson and Cook [33], has been commonly used in performing FE cutting simulation because of its simple multiplicative structure, as shown in Eq. (1). This equation consists of three independent terms, which relate the flow stress σ to the mechanical and thermal loads on the equivalent plastic strain ϵ_p , strain rate $\dot{\epsilon}_0$, and temperature parameters: T (experimental temperature), T_0 (reference temperature), and T_{melt} (melting temperature of the material).

$$\sigma = (A + B\epsilon_p^n)(1 + C \ln \frac{\dot{\epsilon}}{\dot{\epsilon}_0}) \left[1 - \left(\frac{T - T_0}{T_{melt} - T_0} \right)^m \right] \quad (1)$$

In the first term, parameters of A and B are the initial flow stress and the hardening modulus of the material, and n is the work-hardening exponent. In the second term, C represents the work-hardening exponent of the material. And in the third term, m is the thermal softening coefficient of the material. In order to well govern the characteristics of PTFE, A , B , n , C , and m need to be identified experimentally. The quasi-static tension tests were performed to identify the parameters of A , B , and n . And the SHPB tests were conducted to identify the parameters of C and m .

2.1 Quasi-static Tension Tests

The quasi-static tension tests were carried out on the electronic universal test machine, as shown in Fig. 1. The lower die of the machine is fixed and the upper die could move at a constant speed to ensure a constant strain rate during the test. The tension specimens were installed between the two dies. The specimens were prepared according to standard “ASTM D4894”, as shown in Fig. 1. The strain rates were set as: 0.001, 0.005, 0.01, 0.05, and 0.1 s^{-1} . The tests were carried out at room temperature, which was 24°C .

As shown in Fig. 2, the true strain–stress curves converted from the results obtained directly from the quasi-static tension experiments have been applied to identifying the A , B , and n . The curve of strain rate was 0.001 s^{-1} has been used to fit these three parameters.

2.2 Hopkinson Bar Test

As shown in Fig. 3, the experimental setup of the SHPB test consists of the main body, bracket, and acquisition part. The main body consists of the pneumatic pulse generator,

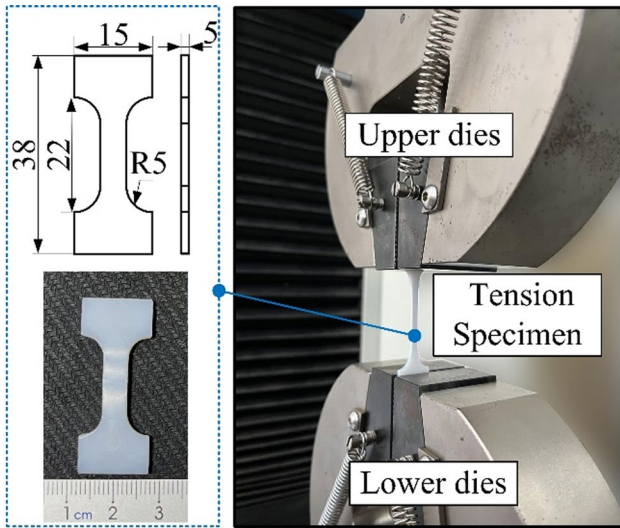


Fig. 1 Experimental set up of tension tests at quasi-static conditions

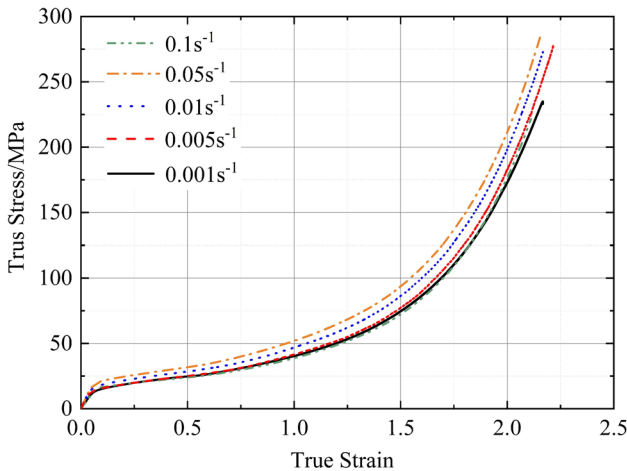


Fig. 2 True strain–stress curves of PTFE at different strain rates

projectile, input bar, output bar, and damper. The specimens are positioned between the input and the out bar. The projectile would be accelerated by the compressed air generated by the pneumatic pulse generator and shoot onto the input bar. The mechanical impulse would be generated at the projectile and input bar interface. This impulse would pass through the input bar. Then, some of the impulses would be reflected by the specimen, while others pass through the specimen leading to deformation. After that, part of the passed impulse would be reflected by the end of the specimen and the remaining would transfer to the output bar. These impulse signals would be transferred to the acquisition system by the strain gauges installed on the bars and, at last, analyzed by the software.

Table 1 summarizes the results of the values of A , B , n , C , and m of the PTFE, which were fitted from the true

Table 1 Material parameter of J–C model for PTFE

Initial flow stress A in MPa	Pre-exponential factor B in MPa	Work hardening exponent n	Strain rate factor C	Thermal softening exponent m
12.52	28.85	1.103	0.1013	0.4725

strain–stress curves obtained by the experiments of quasi-static tension and the SHPB tests.

The recommended aspect ratio of metal specimens for the SHPB test is 1:1 to 1:2. In this paper, PTFE specimens with various geometries have been tested, and it was found that the most stable impulse signals were obtained when using PTFE specimens have a length l_s of 5 mm and a diameter φ of 10 mm (aspect ratio of 1:2). So, the PTFE specimens with the above-mentioned dimension were used to perform SHPB test under different conditions. Generally, the cutting temperature of the PTFE material cutting process varies from 20 to 100 °C [34, 35]. In order to accurately fit the thermal softening exponent m in the J–C constitutive model of PTFE material, SHPB tests with different strain rates were carried out under 24 °C, 50 °C, and 100 °C. The strain rates were set as 500, 1000, 2000, and 3000 s⁻¹. Figure 4 shows the results of the true strain–stress curves of PTFE obtained by SHPB tests under different conditions.

Table 1 summarized the results of the values of A , B , n , C , and m of the PTFE, which were fitted from the true strain–stress curves obtained by the quasi-static tension tests and the SHPB tests.

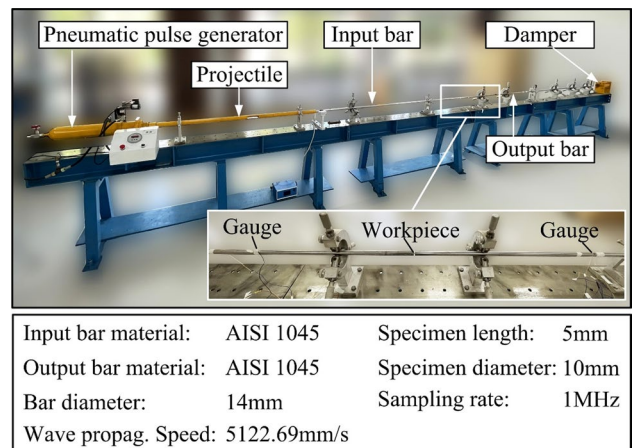


Fig. 3 Experimental set up for SHPB test

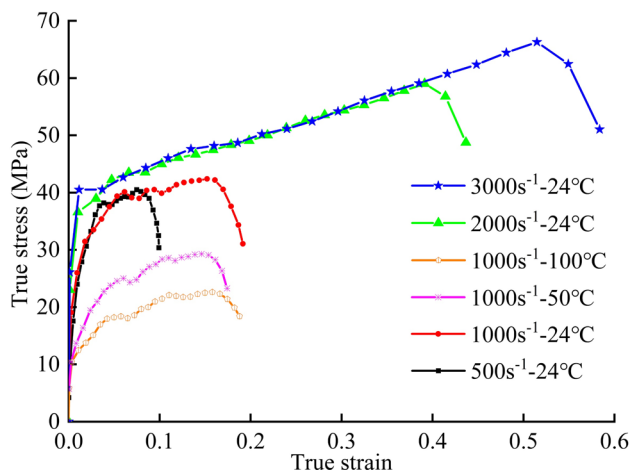


Fig. 4 True strain–stress curves of PTFE obtained from SHPB tests at different strain rates and temperatures

3 Cutting Simulation

To investigate the MUCT of PTFE by the FE simulation, a two-dimensional orthogonal cutting FE simulation is developed using the Abaqus Explicit, as shown in Fig. 5. The unit system SI (mm) was adopted during the modeling.

The dimension of the workpiece were 1 mm in height and 20 mm in length. The basic properties of the workpiece involved in the simulation process are shown in Tables 1 and 2. To ensure the accuracy of the cutting simulation, the four-node plane strain elements (CPE4RT) method has been used to mesh the workpiece, and the mesh size for the cutting area of the workpiece is $5\ \mu\text{m} \times 5\ \mu\text{m}$, while the mesh size for the rest area of the workpiece is $20\ \mu\text{m} \times 20\ \mu\text{m}$. Based on the existing literature and the previous studies, to investigate and

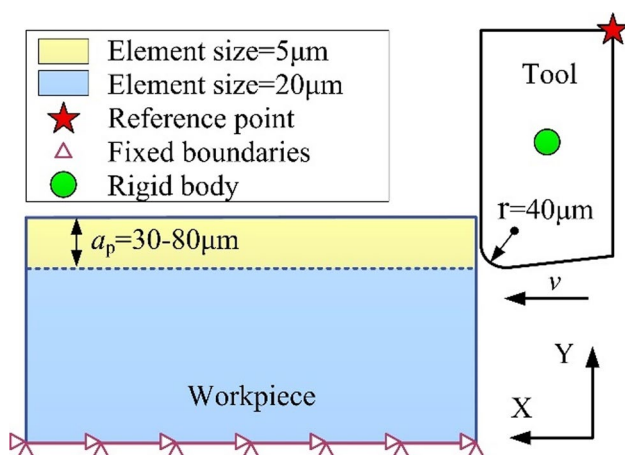


Fig. 5 Schematic of geometry and boundary conditions in FE simulations

Table 2 Physical properties of PTFE

Density (t/mm^3)	2.1e^{-9}
Young's Modulus (MPa)	280
Poisson's Ratio	0.46
Melting temperature ($^{\circ}\text{C}$)	327
Specific Heat ($\text{mJ}\cdot\text{t}^{-1}\cdot\text{K}^{-1}$)	1.05e^9
Conductivity ($\text{mW}\cdot\text{mm}^{-1}\cdot\text{K}^{-1}$)	0.292
Coefficient of linear expansion	$10 \times 10^{-5}/^{\circ}\text{C}$

predict the cutting deformation more accurately, the rake angle, flank angle, and the tool radius of the cutting insert were 0° , 6° , and $40\ \mu\text{m}$, respectively [30–32]. PTFE is much softer than the tool material so the deformation of the tool during the cutting process could be ignored. Therefore, the cutting insert is modeled as a rigid body.

During the simulation, the distance between the workpiece and the tool in the X direction was $2\ \mu\text{m}$. The relative position of the tool varied in the Y direction from 30 to $80\ \mu\text{m}$ according to the cutting depth. In addition, the cutting temperature increase during the orthogonal cutting of PTFE material is minimal due to limited interaction between the tool-workpiece-chip interface, as well as the brief duration of the cutting process [36]. The orthogonal cutting test of PTFE material in this study was carried out at a room temperature of $24\ ^{\circ}\text{C}$. Therefore, in the cutting simulation process, the initial temperature of the simulation is set to $24\ ^{\circ}\text{C}$. In the analysis step, the time period is set as 0.12 according to the cutting length and cutting speed, the target time increment of mass scaling is set as 1e^{-6} , and the max time increment is set as unlimited.

The nodes of the bottom boundary of the workpiece are fixed in both the X and Y directions. Both the contact conditions between the tool interface-workpiece and tool interface-chip were set as surface-to-surface contact (Explicit). The normal behavior and tangential behavior are described with hard contact and penalty models respectively. The coefficient of friction μ is set as 0.02. In order to avoid the impact of chip embedding on the workpiece surface after curling, the contact condition of the chip surface is set to self-contact, and the contact model is set to “Frictionless”.

The tool applied a cutting speed of $5000\ \text{mm}/\text{min}$ along the X direction, which corresponds to the cutting test, and the cutting parameters are listed in Table 3. The cutting force is collected by the reference point (RP) set on the up edge of the tool.

Table 3 Cutting parameters

Cutting parameters	Value
Cutting depth (μm)	30, 40, 50, 60, 70, 80
Cutting speed (mm/min)	5000
Cutting length (mm)	20

4 Cutting Experiment

To investigate the MUCT of PTFE by experiments and validate the established FE cutting model, the orthogonal cutting experiments have been conducted on a turning-milling machine, as shown in Fig. 6. The workpieces have the dimension of 80 mm in length and 30 mm in diameter are purchased from VALQUA (Shanghai) Co. Ltd, and the properties of the workpiece are listed in Table 2. The high-speed steel (HSS) groove cutting insert was used to perform the orthogonal cutting. The rake angle γ , flank angle α , and inclination angle λ of the cutting tool are 0° , 6° , and 0° , respectively. Moreover, the cutting insert was cut open along the cutting edge utilizing wire electrical discharge machining and then polished to measure the tool nose ratio r . It has a radius of $40\ \mu\text{m}$, as shown in Fig. 6b.

This study aims to determine the MUCT of PTFE through orthogonal cutting tests utilizing an orthogonal cutting tool. In the experiment, the orthogonal cutting depth is small, specifically $\leq 0.1\ \text{mm}$. The accuracy of the experimental results is directly affected by whether the orthogonal cutting experiments with different cutting depths could be carried out accurately. In this regard, a particular scheme for the orthogonal cutting experiment is devised. The experimental

procedure for orthogonal cutting consists of three steps: the initial two steps involve the use of a turning tool and a face milling tool to prepare the surface for the orthogonal cutting tests, while the third step entails the actual orthogonal cutting process on the prepared surface, as shown in Fig. 7. The details of the experimental procedure are as follows:

Step 1: the cylindrical PTFE workpiece is clamped by the three-jaw chuck and the outer circumference of the workpiece is machined by the turning tool to maintain the concentricity between the workpiece and the machine spindle.

Step 2: the machine executes the instruction to switch the turning tool to the surface milling tool installed on the power head. The surface milling tool is used to process a surface of 30 mm in length and 20 mm in width. During the surface milling operation, the machine spindle is fixed, as shown in Fig. 7a.

Step 3: the machine executes the instruction to switch the surface milling tool to the orthogonal cutting tool. The surface obtained from step 2 is taken to perform the orthogonal cutting tests, and the machine spindle is fixed, as shown in Fig. 7b.

The purpose of machining the plane used for orthogonal cutting experiment through the aforementioned steps is that the orthogonal cutting tool only needs to be replaced by rotating the tool tower during the orthogonal cutting experiment, and the tool is calibrated from the aspect of numerical control program without manual leveling. The relative position between the tool and the plane would be guaranteed by the machining accuracy ($0.001\ \text{mm}$) and positioning accuracy ($0.001\ \text{mm}$) of the machine tools in the third step. Finally, the sequential execution of the orthogonal cutting experiment with varying cutting depths is conducted. Each cutting depth experiment necessitates the substitution of a new workpiece, and aforementioned steps are reiterated. The key cutting parameters are consistent with the FE simulation

Fig. 6 Experimental set up for the orthogonal cutting tests

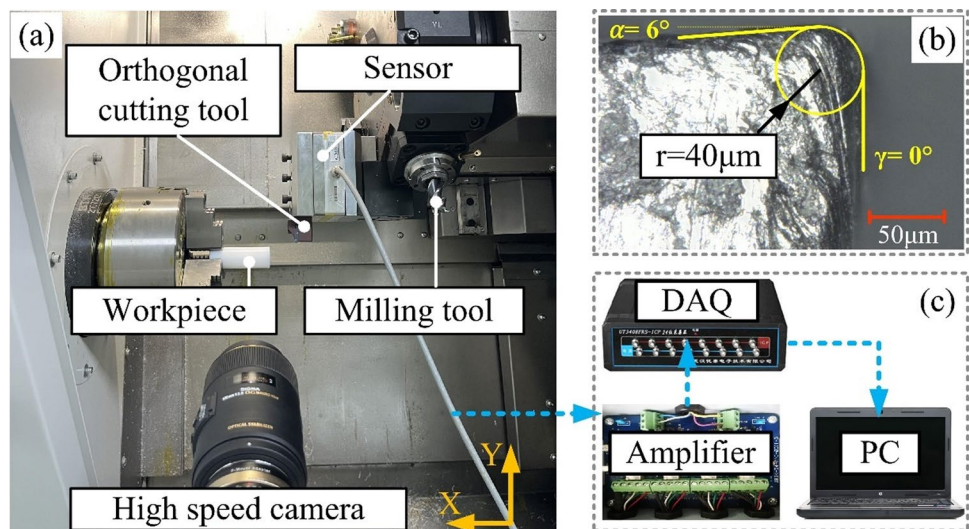
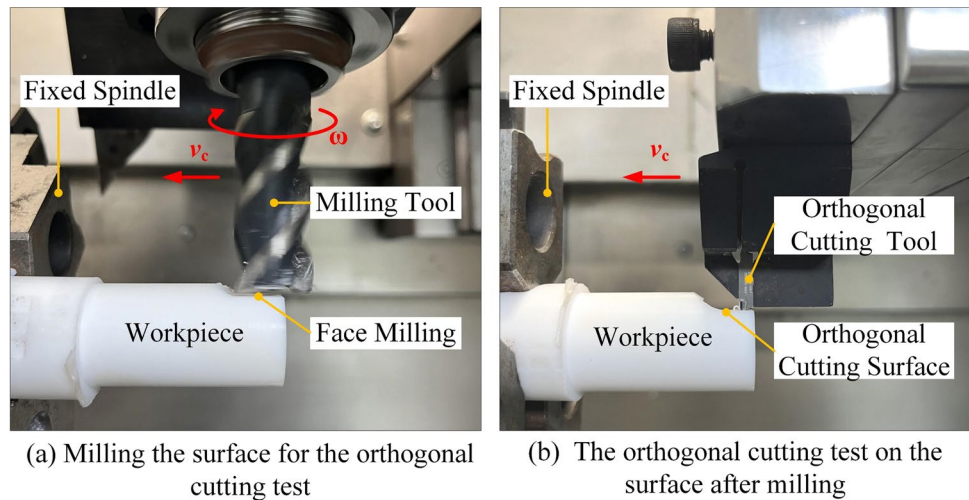


Fig. 7 Scheme of the orthogonal cutting tests



conducted previously. So, the MUCT of PTFE and the accuracy of the FE model could be analyzed directly.

The cutting force signals are collected by the 3-axis force sensor (ME-K3D120) with a sampling frequency of 1 kHz. The measuring range, accuracy, and relative linearity of the force sensor are ± 1 KN, 0.1%, and 0.2%FS respectively. The collected signals are transmitted to the amplifier and analyzed by the data acquisition system (DAQ, uT3408FRS), which has a 24-bit resolution, 8-channel analog, and 2-channel key phase, as shown in Fig. 6c. The orthogonal cutting processes were recorded by the high-speed camera.

5 Results and Discussion

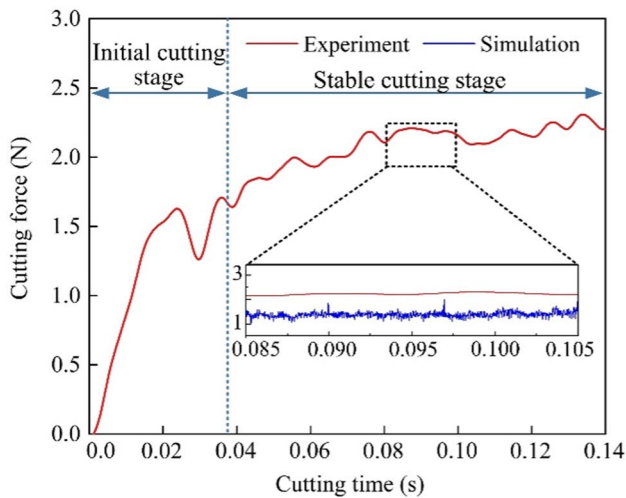
5.1 Validation of the FE Model

The results of the main cutting force F_x obtained from the orthogonal cutting tests and corresponding FE cutting simulations have been compared and analyzed to validate the accuracy of the FE model. Figure 8a depicts the main cutting force curve with cutting time when the cutting depth was 30 μm . The cutting force increased rapidly and then became stable. So, it was divided into the initial cutting stage and the stable cutting stage. In the stable cutting stage, the cutting force signal from (0.085–0.105 s) was selected to perform the comparison. As demonstrated in Fig. 8a, both the cutting force signal from the experiment and FE simulation fluctuate around 1–3 N. The cutting force signal obtained from the cutting simulation is more pronounced than that of the experiment. This could be attributed to that the output frequency of the simulation is higher than the sampling frequency of the sensor used in the experiment.

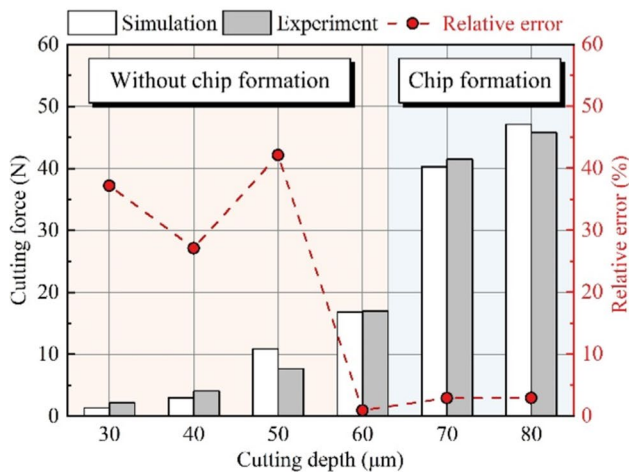
Figure 8b depicts the variation of average cutting force obtained from the stable cutting stage from simulations and experiments with different cutting depths. The average

cutting forces increased with the cutting depth. The minimum relative error between the simulation and experiment was 0.885%, which was obtained in the case of cutting depth was 60 μm . The maximum relative error was 42.1%, which was obtained in the case of a cutting depth was 50 μm . And the relative errors of cutting depth of 30 to 50 μm are larger than those of cutting depths varying from 60 to 80 μm . The large relative errors could be attributed to that when the cutting depth varies from 30 to 50 μm , the cutting force is small, and the simulation is performed under ideal conditions. Any disturbance in the actual cutting tests such as cutting vibration or machine vibration could lead to obvious changes in cutting force [37]. When cutting with the ap of 60 to 80 μm , the cutting force was large enough so that the effect of disturbance decreased. According to the experimental results, the chips were generated when ap was 70 and 80 μm . The relative errors in these two conditions were 2.89% and 2.9%, respectively, which indicated that the established FE model of the PTFE cutting process has high accuracy.

Furthermore, the chip curvature could present the chip formation characteristic during the cutting process. Comparing the chip axial ratio obtained from the cutting simulations and the cutting experiments could evaluate the accuracy of the FE cutting model [25]. The chip morphology obtained in the case of ap was 70 and 80 μm are shown in Fig. 9. Chips in both conditions were continuous. The value of the axial ratio was 1.186, 1.223, and 1.109, 1.132 respectively, and the deviations of 3.03% and 2.03% in the two conditions indicate that the established FE model of the PTFE cutting process has high accuracy. So, considering the results of cutting force and chip formation, the proposed FE model could be applied to predicting the cutting process of PTFE.



(a) Cutting force curves of cutting experiment and simulation when $a_p = 30\mu\text{m}$



(b) Average cutting force of cutting experiment and simulation with different cutting depths.

Fig. 8 Comparison of the main cutting force obtained from the experiment and FE cutting simulation under different conditions

5.2 Analysis of the Minimum Cutting Depth for PTFE

5.2.1 Analysis of the Minimum Cutting Depth by Cutting Force

The characteristics of the cutting process could be determined by analyzing the cutting force, so as to determine the MUCT of PTFE. As shown in Fig. 8b, the average values of F_x increased with the cutting depth. When the cutting depth varies from 30 to 60 μm , the cutting force increases

slowly, and the cutting force increases rapidly when the cutting depth reaches 70 μm . At last, the increasing trend of the cutting force became slow again when the cutting depth varied from 70 to 80 μm .

In this study, no chips were observed when the a_p was 30 μm to 60 μm . The chips generated in the case of a_p were 70 μm and 80 μm , as shown in Fig. 9. In the case of cutting with small a_p (30 μm to 60 μm), the tool face mainly applied friction and extrusion to the workpiece surface. The friction and extrusion generated in the workpiece-tool contact area increased with the cutting depth. The cutting force increased slowly. When a_p reached 70 μm , the chip was generated. The cutting force consisted of friction force, extrusion, and resistance force during the chip formation. And the resistance force is much larger than the other two kinds of forces. So, the cutting force increased rapidly.

5.2.2 Analysis of the Minimum Cutting Depth by the Morphology of the Machined Surface

The contact state between the workpiece-tool surface could be reflected directly by the morphology of the machined surface. So, it is introduced to analyze the minimum cutting thickness of PTFE material indirectly. Figure 10 shows the machined surface under different cutting conditions captured by the confocal laser scanning microscope.

The orthogonal cutting experiment in this study was carried out on the surface of the workpiece after milling. And the orthogonal cutting direction was consistent with the milling direction. It was observed that the friction traces and original milling traces were the dominant characteristics on the machined surface in the cases of the cutting depth varying from 30 to 60 μm , as shown in Fig. 10a–d. When the cutting depth is less than the MUCT, the interaction between the tool and the workpiece surface is mainly friction and extrusion. No materials were removed from the workpiece, the original milling traces could be observed on the machined workpiece surface, and the friction marks are appeared as grooving marks along the orthogonal cutting direction [38].

Based on experimental findings, it was observed that the removal of workpiece material and formation of chips occurred when the cutting depth reached 70 μm . Analysis of Fig. 10e revealed the disappearance of original milling traces on the machined surface, with the appearance of both friction and cutting traces. Further examination in Fig. 10f indicated that cutting traces became more obvious as the cutting depth increased to 80 μm , and the cutting traces are in “wave” shapes. When the cutting depth approaches or exceeds the MUCT, some or all of the original milling traces are removed with the removal of the material under the action of the cutting tool. The “wave” shapes on the machined surface could be attributed to the accumulation

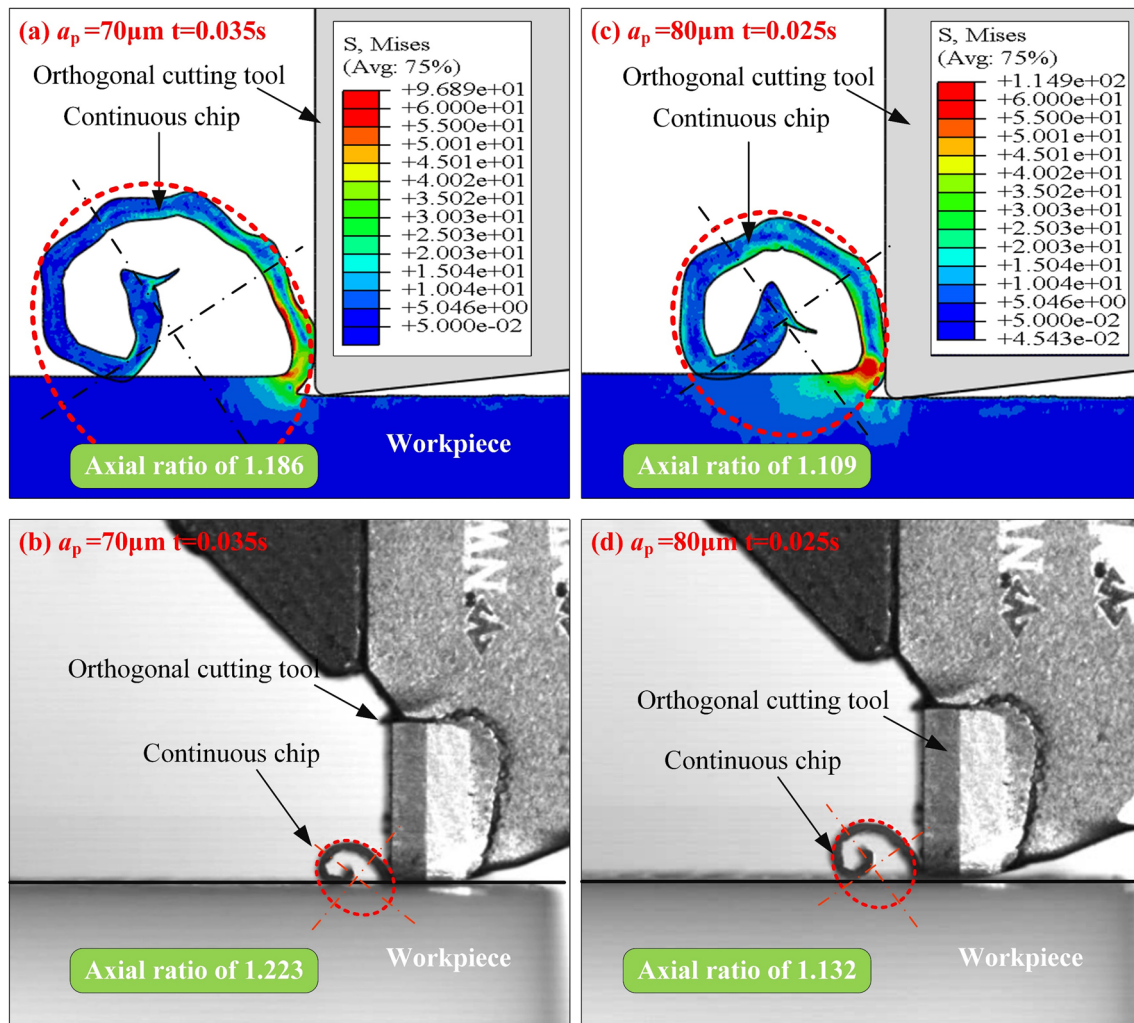


Fig. 9 Chip morphology obtained from the FE cutting simulation and the orthogonal cutting experiment

of the material. This results in the gathering of workpiece surface material towards the tool rake face, ultimately leading to the formation of chips as the material separates from the workpiece. So, the machined surface would have a wavy morphology with the repetition of the above-mentioned process.

5.2.3 Analysis of the Minimum Cutting Depth by the Visualization Results of the Simulation

Based on the comparative analysis of cutting force and chip formation characteristics in numerical and experimental processes, the constitutive model and cutting simulation model developed in this study for PTFE material exhibit a high level of accuracy. Consequently, this section undertakes an analysis of the MUCT of PTFE material by the visualized outcomes obtained from the cutting simulation. According to the results of cutting force, chip formation and surface

morphology, the MUCT of PTFE material in this study is approximately $70\mu\text{m}$. Therefore, the visualized outcomes of cutting simulation with cutting depth of $30\mu\text{m}$, $50\mu\text{m}$ and $70\mu\text{m}$ were selected for comparison and analysis.

During cutting operation, variations in cutting depth directly impact the stress levels within the workpiece-tool-chip interface. Given the stress-sensitive nature of polymer materials, an increase in cutting thickness results in the change of force generated in the cutting area, consequently influencing chip morphology [39]. Experimental findings in this study reveal that upon reaching the MUCT, continuous chips are produced during the orthogonal cutting of PTFE material. So, the Mises stress within the tool-workpiece contact area during the initial stage of orthogonal cutting in three different cutting conditions has been investigated, as shown in Fig. 11a–f.

During cutting operation, variations in cutting depth directly impact the stress levels within the

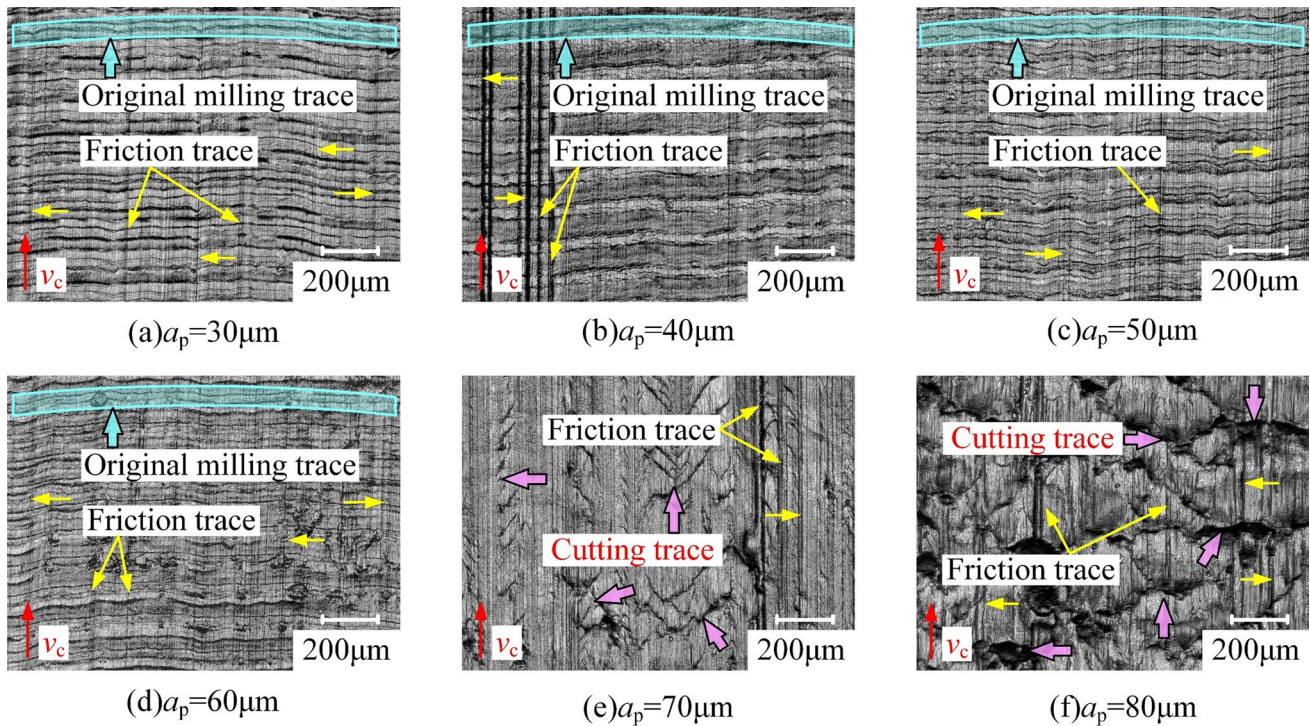


Fig. 10 Morphology of the machined surface under different cutting depth

workpiece-tool-chip interface. Given the stress-sensitive nature of polymer materials, an increase in cutting thickness results in the change of force generated in the cutting area, consequently influencing chip morphology [23]. Experimental findings in this study reveal that upon reaching the MUCT, continuous chips are produced during the orthogonal cutting of PTFE material. So, the Mises stress within the tool-workpiece contact area during the initial stage of orthogonal cutting in three different cutting conditions has been investigated, as shown in Fig. 11a–f.

In the initial cutting stage (5×10^{-4} s), the Mises stress in three conditions was mainly distributed near the tool tip. With the continuation of the cutting process (2×10^{-3} s), under the condition of cutting depth was $30 \mu\text{m}$, the tool and workpiece surface experience interaction in the form of extrusion and friction. The stress is mainly distributed in the area below the workpiece surface-tool contact surface, as shown in Fig. 11d. Combined with the morphology of the machined surface, it can be seen that when the cutting depth is much less than the minimum cutting thickness ($30 \mu\text{m}$), the workpiece surface material will mainly undergo elastic deformation or elastoplastic deformation under the action of the tool, which mainly depends on the material Young's modulus, material yield strength, and tool radius [39]. Due to the small elastic modulus and the low stiffness of PTFE, the surface of PTFE workpiece will undergo elastoplastic deformation under the friction and extrusion of the tool, and

there is no material separation in the case of cutting depth was $30 \mu\text{m}$, as shown in Fig. 11d.

Similarly, as shown in Fig. 11e, when the cutting depth is increased to $50 \mu\text{m}$, the workpiece surface material is mainly subjected to elastic deformation by the extrusion and friction of the tool. Although the small cracks were generated between the workpiece surface material and the workpiece, these cracks had not expanded. Therefore, no chip generated under this condition. When the cutting depth is increased to $70 \mu\text{m}$, as shown in Fig. 11f, cracks were generated between the workpiece surface material and the workpiece. And the stress is mainly concentrated between the workpiece surface material and the front tool face. Under the action of the tool movement, the cracks continued to expand, resulting in the separation of the surface material from the workpiece, and eventually the formation of chips. The plastic deformation of the back side of the chip is greater than that of the front side of the chip under the interaction between the workpiece-tool-chip, so a continuous curly chip is formed. In order to further study the cutting characteristics of PTFE material when the cutting depth is close to the MUCT, the node displacement information from the cutting simulation results is introduced to analyze the interaction between the tool-workpiece-chip interface [40].

Figure 11g–i illustrates the displacement vector diagram of workpiece surface nodes under three cutting depth conditions at 2×10^{-3} s. In Fig. 11g, when the cutting depth is $30 \mu\text{m}$, the

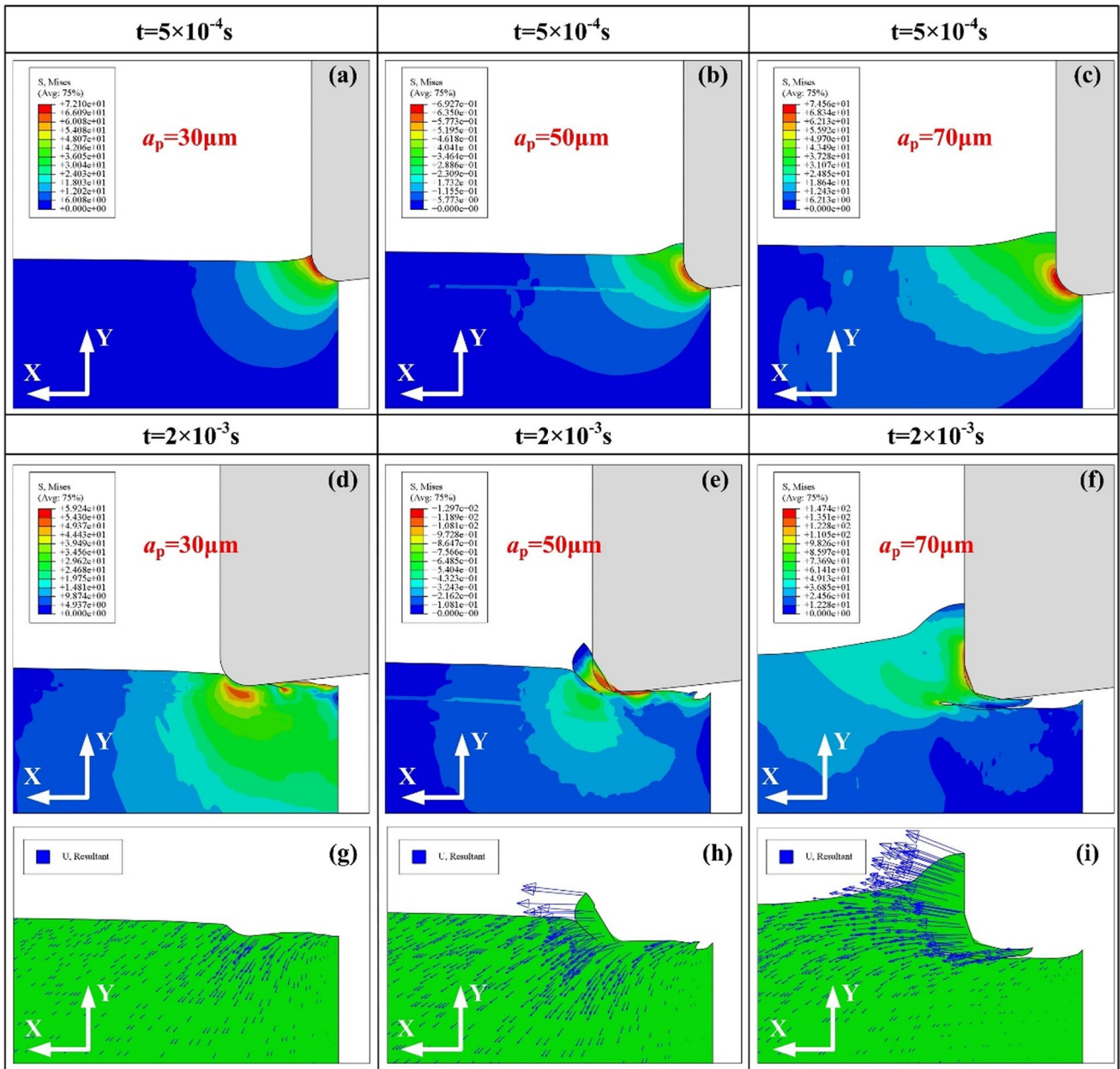


Fig. 11 Visualized outcomes of cutting simulation with cutting depth of 30 μm, 50 μm and 70 μm

tool exhibits no cutting action, resulting in the deformation of the workpiece surface material in the opposite direction of the Y axis due to the extrusion exerted by the tool. This observation aligns with the aforementioned inference. When the cutting depth is 50 μm, the node displacement of the material separated from the workpiece is consistent with the cutting direction, and most of the remaining node displacement is still affected by the tool extrusion friction, the direction is opposite to the Y direction, as shown in Fig. 11h. At this time, the removed material will be pressed into the bottom of the tool under the action of extrusion friction to the machined surface in the subsequent cutting process. Therefore, under

this working condition, the workpiece surface only experiences elastic–plastic deformation and material flow, without the formation of chips. When the cutting depth increased to 70 μm, as shown in Fig. 11i, it can be observed that the direction of most node displacement is still in the opposite direction of the Y direction. However, the displacement direction of the material nodes separated from the workpiece surface is not completely parallel to the cutting direction, and the component of the displacement vector of these nodes gradually points to the direction of the rake face, indicating that the separated material tends to form chips. In the subsequent cutting process, the

Table 4 Minimum uncut chip thickness obtained from experiment and simulation

Material	Minimum uncut chip thickness (μm)	Cutting tool edge radius (μm)	Tool rake angle ($^\circ$)	Tool flank angle ($^\circ$)
PTFE	70	40	0	6

material separated from the workpiece will gradually generate chips and curl along the rake face under the action of the tool.

According to the analysis above, taking the results of cutting force, the machined surface morphology, and the visualized results of the cutting simulation into consideration, the MUCT for PTFE in this study was proposed to be 70 μm , as listed in Table 4.

6 Conclusions

In the present work, the parameters of the J–C constitutive model of PTFE were identified by the quasi-static tension tests and the SHPB test under various testing conditions. The MUCT of PTFE has been studied by 2D FE orthogonal cutting simulation and the corresponding cutting experiments. The accuracy of the proposed FE model and the MUCT of PTFE have been validated and determined in terms of cutting force, chip formation, morphology of the machined surface, and the visualization results of the simulation. The main conclusions are summarized as follows:

1. By conducting the quasi-static tension tests and the SHPB test under various testing conditions, the parameters of the J–C constitutive of PTFE are identified as: initial flow stress A (MPa):12.52, pre-exponential factor B (MPa): 28.85, work hardening exponent n : 1.103, strain rate factor C : 0.1013, and thermal softening exponent m :0.4725.
2. The proposed FE simulation model is reliable. The numerical results are in good agreement with the experimental results, with a minimum relative error of 0.885% in cutting force and 2.03% in the axial ratio of chip curvature.
3. The MUCT of PTFE was determined to be 70 μm , in the case of cutting speed was 5000 mm/min and the rake angle, flank angle, and tool edge radius of the cutting tool are 0° , 6° , and 40 μm , respectively.
4. The properties and flow direction of the removed workpiece material play a significant role in chip formation under the influence of extrusion and friction in the workpiece-tool-chip contact area. The MUCT of PTFE

exceeds the tool radius, which can be attributed to the high elasticity of PTFE. When the cutting depth falls below the MUCT but remains larger than the tool radius, the material is prone to be plowed beneath the cutting tool surface due to the extrusion force exerted by the tool. Consequently, only material flow occurs without the formation of distinct chips.

Further research will focus on modifying the established FE model, and the influence of the different tool geometries such as tool radius and tool angles on the MUCT of PTFE. Simultaneously, 3D cutting model will be proposed and more physical variables such as temperature will be introduced to the simulation model.

Author Contributions Conceptualization, Jing Ni; Data curation, Zhi Cui and Bokai Lou; Formal analysis, Zhi Cui; Funding acquisition, Jing Ni, Zefei Zhu and Lihua He; Methodology, Zhi Cui, and Lihua He; Resources, Jing Ni; Validation, Zhi Cui, Bokai Lou and Jinda Liao; Roles/Writing-original draft, Zhi Cui and Lihua He; Writing-review & editing, Jing Ni and Lihua He.

Funding This research is financially supported by the National Natural Science Foundation of China (Grant No. 52175395), the National Natural Science Foundation of China (Grant No. U22A20197), and the Open Foundation of the State Key Laboratory of Fluid Power and Mechatronic Systems (Grant No. GZKF-202310).

Declarations

Competing interests The authors declare that they have no competing interests.

References

1. Puts, G. J., Crouse, P., & Ameduri, B. M. (2019). Polytetrafluoroethylene: Synthesis and characterization of the original extreme polymer. *Chemical Reviews*, 119, 1763–1805. <https://doi.org/10.1021/acs.chemrev.8b00458>
2. Poitou, B., Dore, F., & Champomier, R. (2009). Mechanical and physical characterisations of polytetrafluoroethylene by high velocity compaction. *International Journal of Material Forming*, 2, 657–660. <https://doi.org/10.1007/s12289-009-0649-8>
3. Schwertz, M., Lemonnier, S., Barraud, E., Carradò, A., Vallat, M., & Nardin, M. (2014). Consolidation by spark plasma sintering of polyimide and polyetheretherketone. *Journal of Applied Polymer Science*, 131, 40783. <https://doi.org/10.1002/app.40783>
4. Gan, Y., Wang, Y., Liu, K., Han, L., Luo, Q., & Liu, H. (2021). A novel and effective method for cryogenic milling of polytetrafluoroethylene. *International Journal of Advanced Manufacturing Technology*, 112, 969–976. <https://doi.org/10.1007/s00170-020-06332-4>
5. Liu, Z. Q., Shi, Z. Y., & Wan, Y. (2013). Definition and determination of the minimum uncut chip thickness of microcutting. *International Journal of Advanced Manufacturing Technology*, 69, 1219–1232. <https://doi.org/10.1007/s00170-013-5109-4>

6. Liu, X., DeVor, R. E., & Kapoor, S. G. (2006). An analytical model for the prediction of minimum chip thickness in micromachining. *Journal of Manufacturing Science and Engineering*, *128*, 474–481. <https://doi.org/10.1115/1.2162905>
7. Ikawa, N., Shimada, S., & Tanaka, H. (1992). Minimum thickness of cut in micromachining. *Nanotechnology*, *3*, 6. <https://doi.org/10.1088/0957-4484/3/1/002>
8. Malekian, M., Mostofa, M. G., Park, S. S., & Jun, M. B. G. (2012). Modeling of minimum uncut chip thickness in micro machining of aluminum. *Journal of Materials Processing Technology*, *212*, 553–559. <https://doi.org/10.1016/j.jmatprotec.2011.05.022>
9. De Oliveira, F. B., Rodrigues, A. R., Coelho, R. T., & De Souza, A. F. (2015). Size effect and minimum chip thickness in micro-milling. *International Journal of Machine Tools and Manufacture*, *89*, 39–54. <https://doi.org/10.1016/j.ijmactools.2014.11.001>
10. Yun, H. T., Heo, S., Lee, M. K., Min, B.-K., & Lee, S. J. (2011). Ploughing detection in micromilling processes using the cutting force signal. *International Journal of Machine Tools and Manufacture*, *51*, 377–382. <https://doi.org/10.1016/j.ijmactools.2011.01.003>
11. Rezaei, H., Sadeghi, M. H., & Budak, E. (2018). Determination of minimum uncut chip thickness under various machining conditions during micro-milling of Ti-6Al-4V. *International Journal of Advanced Manufacturing Technology*, *95*, 1617–1634. <https://doi.org/10.1007/s00170-017-1329-3>
12. Wojciechowski, S. (2021). Estimation of minimum uncut chip thickness during precision and micro-machining processes of various materials—A critical review. *Materials*, *15*, 59. <https://doi.org/10.3390/ma15010059>
13. Liu, H. G., Xu, X., Zhang, J., Liu, Z. C., He, Y., Zhao, W. H., & Liu, Z. Q. (2022). The state of the art for numerical simulations of the effect of the microstructure and its evolution in the metal-cutting processes. *International Journal of Machine Tools and Manufacture*, *177*, 103890. <https://doi.org/10.1016/j.ijmactools.2022.103890>
14. Ducobu, F., Rivière-Lorphèvre, E., & Filippi, E. (2017). On the importance of the choice of the parameters of the Johnson–Cook constitutive model and their influence on the results of a Ti6Al4V orthogonal cutting model. *International Journal of Mechanical Sciences*, *122*, 143–155. <https://doi.org/10.1016/j.ijmecsci.2017.01.004>
15. Cai, Z., Ji, H., Pei, W., Wang, B., Huang, X., & Li, Y. (2019). Constitutive equation and model validation for 33Cr23Ni8Mn3N heat-resistant steel during hot compression. *Results in Physics*, *15*, 102633. <https://doi.org/10.1016/j.rinp.2019.102633>
16. Kong, J., Zhang, T., Du, D., Wang, F., Jiang, F., & Huang, W. (2021). The development of FEM based model of orthogonal cutting for pure iron. *Journal of Manufacturing Processes*, *64*, 674–683. <https://doi.org/10.1016/j.jmapro.2021.01.044>
17. Seif, C. Y., Hage, I. S., & Hamade, R. F. (2019). Utilizing the drill cutting lip to extract Johnson Cook flow stress parameters for Al6061-T6. *CIRP Journal of Manufacturing Science and Technology*, *26*, 26–40. <https://doi.org/10.1016/j.cirpj.2019.06.001>
18. Lerra, F., Candido, A., Liverani, E., & Fortunato, A. (2022). Prediction of micro-scale forces in dry grinding process through a FEM—ML hybrid approach. *International Journal of Precision Engineering and Manufacturing*, *23*(1), 15–29. <https://doi.org/10.1007/s12541-021-00601-2>
19. Rae, P. J., & Dattelbaum, D. M. (2004). The properties of poly(tetrafluoroethylene) (PTFE) in compression. *Polymer*, *45*(22), 7615–7625. <https://doi.org/10.1016/j.polymer.2005.06.120>
20. Rae, P. J., & Brown, E. N. (2005). The properties of poly(tetrafluoroethylene) (PTFE) in tension. *Polymer*, *46*(19), 8128–8140. <https://doi.org/10.1016/j.polymer.2005.06.120>
21. Yan, L., Jiang, A. N., Li, Y. N., Qiu, T., & Jiang, F. (2022). Dynamic constitutive models of Ti-6Al-4V based on isothermal stress–strain curves. *Journal of Materials Research and Technology*, *19*, 4733–4744. <https://doi.org/10.1016/j.jmrt.2022.06.164>
22. Yang, B., Wang, H., Fu, K., & Wang, C. (2022). Prediction of cutting force and chip formation from the true stress-strain relation using an explicit FEM for polymer machining. *Polymers*, *14*, 189. <https://doi.org/10.3390/polym14010189>
23. Fu, G., Sun, F., Huo, D., Shyha, I., Sun, F., & Fang, C. (2021). FE-simulation of machining processes of epoxy with Mulliken–Boyce model. *Journal of Manufacturing Processes*, *71*, 134–146. <https://doi.org/10.1016/j.jmapro.2021.09.026>
24. Fan, Y., Xu, Y., Hao, Z., & Lin, J. (2022). Cutting deformation mechanism of SiCp/Al composites based on strain gradient theory. *Journal of Materials Processing Technology*, *299*, 117345. <https://doi.org/10.1016/j.jmatprotec.2021.117345>
25. Lu, S. J., Li, Z. Q., Zhang, J. J., Zhang, C. Y., Li, G., Zhang, H. J., & Sun, T. (2022). Coupled effect of tool geometry and tool-particle position on diamond cutting of SiCp/Al. *Journal of Materials Processing Technology*, *303*, 117510. <https://doi.org/10.1016/j.jmatprotec.2022.117510>
26. Bagheri, B., Abdollahzadeh, A., Abbasi, M., & Kokabi, A. H. (2021). Effect of vibration on machining and mechanical properties of AZ91 alloy during FSP: Modeling and experiments. *International Journal of Material Forming*, *14*(4), 623–640. <https://doi.org/10.1007/s12289-020-01551-2>
27. Teng, X., Xiao, D., & Jiang, X. (2022). Numerical investigation of machining of SiC/Al matrix composites by a coupled SPH and FEM. *International Journal of Advanced Manufacturing Technology*, *122*, 2003–2018. <https://doi.org/10.1007/s00170-022-09985-5>
28. Saelzer, J., Thimm, B., & Zabel, A. (2022). Systematic in-depth study on material constitutive parameter identification for numerical cutting simulation on 16MnCr5 comparing temperature-coupled and uncoupled Split Hopkinson pressure bars. *Journal of Materials Processing Technology*, *302*, 117478. <https://doi.org/10.1016/j.jmatprotec.2021.117478>
29. Elkaseer, A., Abdelaziz, A., Saber, M., & Nassef, A. (2019). FEM-based study of precision hard turning of stainless steel 316L. *Materials*, *12*, 2522. <https://doi.org/10.3390/ma12162522>
30. Xu, X., Outeiro, J., Zhang, J., Xu, B., Zhao, W., & Astakhov, V. (2021). Machining simulation of Ti6Al4V using coupled Eulerian–Lagrangian approach and a constitutive model considering the state of stress. *Simulation Modelling Practice and Theory*, *110*, 102312. <https://doi.org/10.1016/j.simpat.2021.102312>
31. Ribeiro, C. S., Horovistiz, A., & Davim, J. P. (2021). Material model assessment in Ti6Al4V machining simulations with FEM. *Proceedings of the Institution of Mechanical Engineers, Part C: Journal of Mechanical Engineering Science*, *235*(21), 5500–5510. <https://doi.org/10.1177/0954406221994883>
32. Daoud, M., Chatelain, J. F., & Bouzid, A. (2017). Effect of rake angle-based Johnson–Cook material constants on the prediction of residual stresses and temperatures induced in Al2024-T3 machining. *International Journal of Mechanical Sciences*, *122*, 392–404. <https://doi.org/10.1016/j.ijmecsci.2017.01.020>
33. Johnson, G. R., & Cook, W. H. (1983). A constitutive model and data for metals subjected to large strains, high strain rates and high temperatures. In *Proceedings of the 7th International Symposium*

- on *Ballistics*. Royal Netherlands Society of Engineers, Den Haag Nederlande (pp. 541–547).
34. Cui, Z., Ni, J., He, L., Su, R., Wu, C., Xue, F., & Sun, J. (2022). Assessment of cutting performance and surface quality on turning pure polytetrafluoroethylene. *Journal of Materials Research and Technology*, 2022(20), 2990–2998. <https://doi.org/10.1016/j.jmrt.2022.08.075>
 35. Ni, J., Lou, B., Cui, Z., He, L., & Zhu, Z. (2022). Assessment of turning polytetrafluoroethylene external cylindrical groove with curvilinear profile tool. *Materials*, 16(1), 372. <https://doi.org/10.3390/ma16010372>
 36. Cui, Z., Ni, J., He, L., Guan, L., Han, L., & Sun, J. (2022). Investigation of chip formation, cutting force and surface roughness during orthogonal cutting of polytetrafluoroethylene. *Journal of Manufacturing Processes*, 77, 485–494. <https://doi.org/10.1016/j.jmapro.2022.03.031>
 37. Jiao, A., Yuan, J., Zhang, Y., Zhang, J., Miao, Y., & Liu, G. (2023). Study on variable parameter helical milling of TC4 titanium alloy tube. *International Journal of Precision Engineering and Manufacturing*, 24(11), 1947–1959. <https://doi.org/10.1007/s12541-023-00865-w>
 38. Gong, L., Bertolini, R., Bruschi, S., Ghiotti, A., & He, N. (2022). Surface integrity evaluation when turning Inconel 718 alloy using sustainable lubricating-cooling approaches. *International Journal of Precision Engineering and Manufacturing-Green Technology*, 9(1), 25–42. <https://doi.org/10.1007/s40684-021-00310-1>
 39. Wang, G., Yu, T., Zhou, X., Guo, R., Chen, M., & Sun, Y. (2023). Material removal mechanism and microstructure fabrication of GDP during micro-milling. *International Journal of Mechanical Sciences*, 240, 107946. <https://doi.org/10.1016/j.ijmecsci.2022.107946>
 40. Shi, Z. Y., Li, Y. C., Liu, Z. Q., & Qiao, Y. (2018). Determination of minimum uncut chip thickness during micro-end milling Inconel 718 with acoustic emission signals and FEM simulation. *International Journal of Advanced Manufacturing Technology*, 98, 37–45. <https://doi.org/10.1007/s00170-017-0324-z>

Publisher's Note Springer Nature remains neutral with regard to jurisdictional claims in published maps and institutional affiliations.

Springer Nature or its licensor (e.g. a society or other partner) holds exclusive rights to this article under a publishing agreement with the author(s) or other rightsholder(s); author self-archiving of the accepted manuscript version of this article is solely governed by the terms of such publishing agreement and applicable law.



Zhi Cui He is a doctoral student in the School of Mechanical Engineering, Hangzhou Dianzi University. His research interests include high-performance manufacturing technology of complex components of integrated circuits, and Precision manufacturing technology.



technology of complex components of integrated circuits, aerospace and nuclear power.

Jing Ni He received his B.S. degree in mechanical engineering and automation in 2000 from Liaoning Petrochemical University, Liaoning, China. He received his M.S. degree and Ph.D. degree in mechanical engineering and automation from Zhejiang University, Hangzhou China. His current position is a professor and doctoral supervisor of School of Mechanical Engineering, Hangzhou Dianzi University. His research areas cover the research of high-performance manufacturing technology



Lihua He He received his M.S. and Ph.D. degrees in mechanical engineering from Hunan University, China, in 2012 and 2017, respectively. He is currently a professor in Hangzhou Dianzi University. His research interests include high-performance manufacturing technology of complex components of integrated circuits, and precision manufacturing technology.



complex components of integrated circuits, aerospace and nuclear power.

Zefei Zhu He received his B.S. degree in mechanical engineering in 1983 from Harbin Institute of Shipbuilding Technology, Harbin, China. He received his M.S. degree and Ph.D. degree in mechanical engineering and automation from Zhejiang University, Hangzhou China. His current position is a professor and doctoral supervisor of School of Mechanical Engineering, Hangzhou Dianzi University. His research areas cover the research of high-performance manufacturing technology of



Bokai Lou is a doctoral student in the School of Mechanical Engineering, Hangzhou Dianzi University. His current research interests include high-performance manufacturing, multi-scale mechanics, and precision machining.



Jinda Liao is an undergraduate student in the School of Mechanical Engineering, Hangzhou Dianzi University. His current research interest including polymer machining, high-performance manufacturing.